Original Article

JCBFM

Journal of Cerebral Blood Flow & Metabolism
0(0) 1–14

DOI: 10.1177/0271678X221108841
journals.sagepub.com/home/jcbfm

Quantitative kinetic modelling and mapping of cerebral glucose transport and metabolism using glucoCESL MRI

Ben R Dickie[1,2], Tao Jin[3], Ping Wang[3], Rainer Hinz[4], William Harris[1,2], Hervé Boutin[1,2], Geoff JM Parker[5,6], Laura M Parkes[1,2] and Julian C Matthews[1,2]

Abstract

Chemical-exchange spin-lock (CESL) MRI can map regional uptake and utilisation of glucose in the brain at high spatial resolution (i.e sub 0.2 mm^3 voxels). We propose two quantitative kinetic models to describe glucose-induced changes in tissue $R_{1\rho}$ and apply them to glucoCESL MRI data acquired in tumour-bearing and healthy rats. When assuming glucose transport is saturable, the maximal transport capacity (T_{max}) measured in normal tissue was 3.2 ± 0.6 μmol/min/mL, the half saturation constant (K_t) was 8.8 ± 2.2 mM, the metabolic rate of glucose consumption (MR_{glc}) was 0.21 ± 0.13 μmol/min/mL, and the cerebral blood volume (v_b) was 0.006 ± 0.005 mL/mL. Values in tumour were: $T_{max} = 7.1 \pm 2.7$ μmol/min/mL, $K_t = 14 \pm 1.7$ mM, $MR_{glc} = 0.22 \pm 0.09$ μmol/min/mL, $v_b = 0.030 \pm 0.035$ mL/mL. T_{max} and K_t were significantly higher in tumour tissue than normal tissue ($p = 0.006$ and $p = 0.011$, respectively). When assuming glucose uptake also occurs via free diffusion, the free diffusion rate (k_d) was 0.061 ± 0.017 mL/min/mL in normal tissue and 0.12 ± 0.042 mL/min/mL in tumour. These parameter estimates agree well with literature values obtained using other approaches (e.g. NMR spectroscopy).

Keywords

GlucoCESL, glucoCEST, cerebral glucose metabolism, kinetic modelling, brain tumours

Received 3 August 2021; Revised 23 May 2022; Accepted 25 May 2022

Cerebral glucose metabolism is altered in a range of neurological diseases including brain tumours,[1] Alzheimer's disease,[2] Parkinson's disease,[3,4] and multiple sclerosis.[5,6] The metabolic rate of glucose consumption (MR_{glc}) is dependent on the rate of glucose transport across the blood-brain barrier (BBB) and downstream utilisation by neurons and astrocytes. When the BBB is intact, glucose enters the brain via the GLUT1 glucose transporter located on endothelial cell membranes, and moves into cells primarily via GLUT1 on astrocyte cell membranes and GLUT3 on neuronal cell membranes.[7] Movement of glucose through glucose transporters can be approximated by Michaelis-Menten kinetics, with the rate being saturable and dependent on the half saturation constant (also called the binding constant), K_t, and the maximum transport capacity, T_{max}.[8] Different glucose

[1]Division of Neuroscience and Experimental Psychology, Faculty of Biology, Medicine and Health, The University of Manchester, Manchester, UK
[2]Geoffrey Jefferson Brain Research Centre, Manchester Academic Health Science Centre, Manchester, UK
[3]Department of Radiology, University of Pittsburgh, Pittsburgh, Pennsylvania, USA
[4]Division of Informatics, Imaging, and Data Science, Faculty of Biology Medicine and Health, University of Manchester, Manchester, UK
[5]Bioxydyn Limited, Manchester, UK
[6]Centre for Medical Image Computing, Department of Medical Physics & Biomedical Engineering and Department of Neuroinflammation, University College London, London, UK

Corresponding author:
Ben Dickie, The University of Manchester, Stopford Building, Oxford Road, Manchester, M13 9PL, UK.
Email: ben.dickie@manchester.ac.uk

transporters have different K_t values, and thus *in-vivo* measurement of K_t may provide insight into their relative distribution on cellular membranes and alterations to this distribution caused by disease. The maximum transport capacity depends on the availability of transporters (i.e. their density), and similarly in-vivo measurements of T_{max} could provide important information regarding the effects of ageing or pathology on glucose delivery to the brain.

In some solid tumours, glucose transporter expression is increased,[9] which has been shown to correlate with tumour hypoxia, a property associated with treatment resistance and tumour agressiveness.[10,11] Due to aberrant vessel formation during neo-angiogenesis, BBB integrity may also be compromised, leading to increased free diffusion of glucose across the blood-tumour interface. In neurodegenerative diseases such as Alzheimer's disease, glucose transporter expression is reduced[7,12] which may starve the brain of glucose,[13] and contribute towards neurodegeneration.[14] In many diseases, alterations to glucose transport and/or metabolism are regionally specific, and thus being able to detect glucose transport and utilisation at high spatial resolution across multiple brain regions, would greatly progress our ability to study deficiencies in glucose transport and metabolic dysfunction.

2-deoxy-2-[^{18}F]fluoro-D-glucose positron emission tomography (FDG-PET) is the gold-standard technique for imaging glucose transport and metabolism *in-vivo,* and has led to improved understanding of metabolic dysfunction across a range of brain diseases.[15,16] Typically, trace amounts of FDG are injected and late static tissue PET measurements made. For full kinetic modelling, and in order to derive rates of cerebral glucose transport and utilisation, FDG kinetics in arterial blood and tissue are needed from arterial blood sampling and dynamic PET scanner measurements.[17,18] FDG differs in its transport and phosphorylation properties relative to glucose and the estimated rate constants derived using FDG must be converted to glucose rate constants using an experimentally derived lumped constant.[19,20] Several attempts have been made to measure the lumped constant for FDG, with values ranging from 0.71–0.89[21,22] in rat and 0.68–0.89[20,23–25] in human, presenting a significant potential source of bias. Quantification of glucose metabolic rates in brain tumours using FDG is further complicated by the unknown redistribution of glucose transporters.

Detection of glucose *in-vivo* in the brain is possible using magnetic resonance spectroscopy (MRS), as first reported by Frahm et al. in 1991.[3,26] ^{1}H MRS has been used to measure uptake and utilisation of glucose following hyperglycaemic challenge, measuring changes in the glucose signals at 3.44 and 5.23 ppm.[27–29] However, quantification is difficult due to spectral overlap with more concentrated metabolites such as *myo*-inositol, creatine/phosphocreatine and amino acids. Significant effort has been invested in developing methods to improve the specificity to glucose, and downstream metabolites using ^{13}C-labelling,[27,30–36] and more recently, ^{2}H-labelled glucose.[37–39] In both cases, the label passes down the glycolytic pathway, and can be detected in glucose itself and downstream metabolites such as lactate and glutamate. A key advantage of these approaches is reduced spectral overlap, because unlabelled endogenous molecules do not contribute to the spectra. However, these methods are still limited by low sensitivity, meaning large voxel volumes are required to provide adequate signal to noise for precise quantification. Usually, specialised coils[36] are required for ^{13}C and ^{2}H approaches, limiting translation, though there are approaches to detect the presence of ^{13}C-labelled metabolites in ^{2}HMRS that do not require either a ^{13}C-channel or ^{13}C –tuned RF coil.[40] Nevertheless, this latter approach lacks the sensitivity to detect glucose itself, being limited to detection of the higher concentration downstream metabolite, glutamate.

More recently, chemical exchange saturation transfer (CEST) and chemical-exchange spin lock (CESL) MRI have been used to indirectly detect glucose via chemical exchange of protons in the hydroxyl groups ($^-$OH) of glucose with protons in water. These approaches are derived from techniques that image exchangeable protons in macromolecules[41,42] and more recently have been used to spatially map glucose uptake in living tissues, and appear to overcome the low detection sensitivity limitations of spectroscopic approaches. CEST was first applied to map uptake of intravenously administered glucose in tumours by Chan et al.[43] then Walker-Samuel et al..[44] Since then, CEST and CESL have been applied to detect glucose uptake in rodent and human brain by a number of groups.[45–53] Jin et al.[46] and others[50,54–56] have performed key studies in normal brain, tumour, and stroke showing that glucoCESL and glucoCEST uptake curves are sensitive to both uptake and metabolism of glucose.[50,54] In these studies, the uptake curves of D-glucose and/or glucose-analog 3-O-methyl-D-glucose (3OMG) were monitored using CESL or CEST MRI. D-glucose and 3OMG are taken up by tissues at similar rates, but 3OMG, which is not metabolised, was found to remain at high levels, while the curves for D-glucose decreased to pre-injection levels. Despite these studies showing the clear sensitivity of CESL and CEST to the transport *and* metabolism of glucose, and the potential for mapping these processes at high spatial resolution, kinetic modelling to determine physiological rate constants has not been applied to this type of data.

In this study, we introduce the theoretical background for quantitative kinetic modelling of glucoCESL MRI data. We evaluate the sensitivity of $R_{1\rho}$ to all kinetic model parameters, evaluate bias introduced due to inaccurate glucose input functions, and apply the models to data acquired in tumour-bearing (9 L glioma) and healthy rats. We evaluate two kinetic models describing purely saturable transport (model 1) and mixed transport with saturable and free diffusion components (model 2). The fit quality of each model is compared using the Akaike information criterion on a voxel wise level. Finally, we evaluate differences in the central tendency and distribution (standard deviation) of estimated transport and metabolic parameters between tumour and normal tissue.

Relaxation model

In the presence of an on-resonant spin-lock pulse, the spin-lock relaxation rate $R_{1\rho}$ can be written in terms of chemical-exchange and non-chemical exchange contributions:[46]

$$R_{1\rho} = R_{ex} + R_{20} \tag{1}$$

where R_{ex} is the contribution due to chemical exchange between labile protons in biomolecules, and protons in water, and R_{20} is the spin-spin relaxation rate of water without chemical exchange contributions.

Following administration of glucose into the bloodstream, the amount of labile proton exchange between hydroxyl groups ($^{-}$OH) in glucose and water will theoretically increase in proportion with the concentration of glucose, leading to an increase in voxel $R_{1\rho}$ via alteration of R_{ex}. The effect of glucose concentration on R_{20} is assumed negligible.

Changes in $R_{1\rho}$ may occur due to increased/decreased proton exchange with glucose or any other detectable (via exchange) metabolic product of glucose, i. We can therefore write the total change in $R_{1\rho}$ as the sum of these contributions:

$$\Delta R_{1\rho} = \sum_i r_i \Delta C_i \tag{2}$$

where ΔC_i is the change in concentration of molecule i (i includes any detectable molecule, including glucose or metabolic products of glucose) and r_i is the $R_{1\rho}$ relaxivity of each of these molecules.

Assuming the population of labile proton i is much smaller than the population of water protons, the relaxivities r_i [(s mM)$^{-1}$] are theoretically dependent on the spin-lock frequency ω_1 (set during the experiment), the resonance frequency gap between molecule i and water, δ_i [s^{-1}] (fixed), the number of labile protons per molecule n, and the exchange rate between these labile protons and water, k_i [s^{-1}] (fixed, but known to vary with tissue pH[46])

$$r_i = \left(\frac{n}{1.11 \cdot 10^5}\right) \frac{k_i \delta_i^2}{\delta_i^2 + 4\pi^2 \omega_1^2 + k_i^2} \tag{3}$$

The factor 1.11×10^5 is the concentration of protons in pure water in units of mM (assuming a pure water concentration of 55 M) and ensures the relaxivity has units of [(s mM)$^{-1}$]. For accurate modelling of the relaxivity, the concentration of water protons in the relevant brain structures should be used if known.

In healthy brain tissue, the majority of glucose undergoes glycolysis. In neurons and astrocytes, glucose is phosphorylated by hexokinase into glucose-6-phosphate (G6P), which at rest inhibits hexokinase activity to maintain a constant metabolic rate of glucose consumption, regardless of tissue glucose concentrations.[57] There may therefore be relatively large fluctuations in G6P following intravenous injection of glucose (in percentage terms), but the basal concentration will remain very low relative to glucose[58] (<2–3%), and therefore these changes will have only a minor effect on measured $\Delta R_{1\rho}$, even if r_i of 6GP is of a similar magnitude to glucose. At resting state, the concentrations of other downstream metabolic products (e.g. glycogen, glutamate) should remain fairly stable[59] and independent of changing tissue glucose levels, and thus should also not contribute to measured $\Delta R_{1\rho}$. In tumours, metabolism is reprogrammed to support anabolic growth in nutrient deplete environments. A key component of this transformation is for tumour cells to convert pyruvate to lactate, which then accumulates extracellularly. Fortunately, for glucoCESL studies, the exchange rate of lactate is much lower than the resonance frequency separation between lactate and water[60] meaning increases in lactate concentration due to increased glucose supply should not contribute significantly to $\Delta R_{1\rho}$ (i.e., $k_i \ll \delta_i$ in equation (3)).

Taken together, we assume that changes in $\Delta R_{1\rho}$ following intravenous glucose injection are predominantly driven by changes in glucose concentration only (i.e. effects of changing metabolite concentrations are negligible). We can therefore rewrite equation (2) to include contributions from glucose only, and rearrange to show how measured $\Delta R_{1\rho}$ can be converted to changes in glucose concentration:

$$\Delta C = \frac{\Delta R_{1\rho}}{r_g} \tag{4}$$

where r_g is the $R_{1\rho}$ relaxivity of glucose, and ΔC is the change in tissue glucose concentration. Hence by tracking dynamic changes in $R_{1\rho}$ we can infer changes in glucose concentration. Kinetic models can be fit to the concentration time-course data to extract quantitative parameters relating to glucose transport and metabolism.

Kinetic models

Two kinetic models are proposed to describe changes in tissue glucose concentration (Figure 1). Both models assume the metabolic rate of glucose consumption, $MR_{\mathrm{glc}} = C_1 \cdot k_3$, is constant, as would be expected at rest. In the brain, glucose is phosphorylated into glucose-6-phosphate primarily by hexokinase I, and then stored intracellularly before being utilised in the glycolytic or pentose-phosphate pathways.[57] Hexokinase exhibits unique regulatory properties, in that its rate of activity is potently inhibited by its product.[57,61] Thus, when glucose-6-phosphate is required by the cell, local glucose-6-phosphate levels become depleted, and the rate of glucose phosphorylation increases to restore glucose-6-phosphate levels (increased k_3). When glucose-6-phosphate levels are high, hexokinase inhibition increases and glucose s.p phosphorylation is reduced (reduced k_3). Thus, when intracellular glucose concentrations are increased (as would occur during an i.v. bolus injection of glucose), the amount of glucose-6-phosphate being produced will momentarily increase, then immediately self-regulate via increased inhibition of hexokinase (reduced k_3).[61] This mechanism ensures that, at rest and at equilibrium, the metabolic rate of glucose consumption MR_{glc} remains constant, even in the presence of increased intracellular glucose levels.

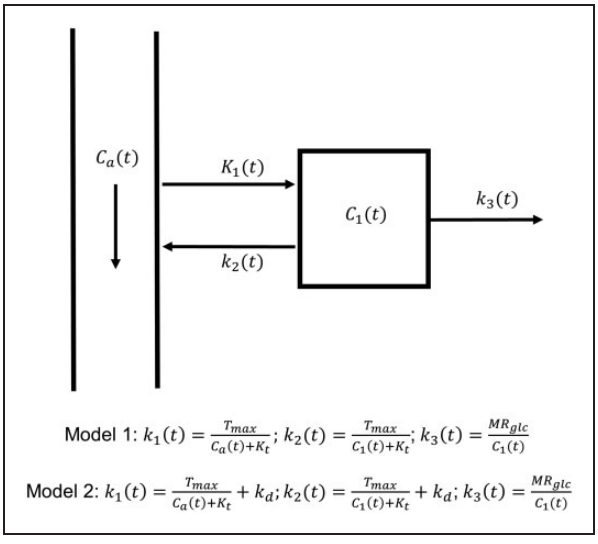

Figure 1. Diagram of the kinetic models. Arterial and tissue glucose have concentrations $C_a(t)$ and $C_1(t)$ respectively. The rate of glucose uptake across an intact blood-brain barrier is modelled with Michaelis-Menten kinetics (model 1), where k_1 is parameterised by the maximal transport capacity T_{max}, half saturation constant K_t, and is dependent on the arterial glucose concentration $C_a(t)$. In addition to transporter mediated uptake, glucose may also freely diffuse across the BBB into tissue with rate constant k_d (model 2). We assume that $k_3(t)$ decreases in response to an increase in $C_1(t)$ to maintain a constant metabolic rate of glucose consumption, MR_{glc} (i.e., $MR_{glc} = k_3(t)C_1(t)$).

Model 1 assumes the influx and efflux rates of glucose across the blood-brain barrier (BBB), K_1 and k_2, are time-dependent and governed by Michaelis-Menten kinetics.[8]

$$K_1(t) = \frac{T_{\max}}{C_a(t) + K_t} \tag{5}$$

$$k_2(t) = \frac{T_{\max}}{C_1(t) + K_t} \tag{6}$$

where $C_a(t)$ [mM], and $C_1(t)$ [mM] are the arterial and tissue glucose concentrations respectively, $T_{\max}$ [μmol/min/mL] is the maximal transport capacity, and K_t [mM] is the half saturation constant of the glucose transporters. Model 2 assumes uptake of glucose is governed by a mixture of Michaelis-Menten kinetics and passive diffusion.[62] An extra term k_d [mL/min/mL] is added to the right-hand side of equations (5) and (6) (see Figure 1). The mass transport equation for both models is:

$$\frac{dC_1(t)}{dt} = K_1(t)C_a(t) - k_2(t)C_1(t) - MR_{glu} \tag{7}$$

Both models are defined diagrammatically in Figure 1. The total glucose concentration in a given brain voxel is modelled as a volume weighted average of blood (capillary) and tissue glucose concentrations:

$$C(t) = v_b C_c(t) + \ (1 - v_b)C_1(t) \tag{8}$$

where v_b [mL mL^{-1}] is the fractional blood volume. The capillary glucose concentration is assumed to be equal to the glucose of the feeding artery ($C_a = C_c$), which is a good assumption in highly perfused tissues such as the brain.[63]

To calculate the change in voxel glucose concentration following intravenous administration of glucose solution, we subtract the modelled baseline glucose concentration:

$$\Delta C(t) = C(t) - C(t = 0) \tag{9}$$

where $C(t = 0)$ can be derived for any compartment model at steady state by assuming $\frac{dC_1(t)}{dt} = 0$.

Derivations of $C(t=0)$ for model 1 and model 2 are given in Supplementary materials.

Sensitivity analysis

Model sensitivity analysis was performed to determine the relative contribution of each model parameter and the rate of glucose clearance from the blood on $\Delta R_{1\rho}$. For both kinetic models, a 50% change in each parameter was simulated using equation (9), and the effect of these changes on $\Delta R_{1\rho}$ curves were plotted using equation (4). The initial values of each parameter from which perturbations were made were based on previously published literature data[31,58,64] and set to $T_{max}=3.3\,\mu$mol/min/mL, $K_t=8.1$ mM, $MR_{glc}=0.3\,\mu$mol/min/mL, $k_d=0.05$ mL/min/mL, $v_b=0.05$ mL/mL. A population level arterial glucose input function, C_a(t), measured in Sprague-Dawley rats was used (see arterial glucose input function section below for details). Sensitivity of tissue $\Delta R_{1\rho}$ to increased (Figure 2(a); dashed yellow line) or decreased (Figure 2(a), dashed black line) glucose clearance from blood was simulated by creating two additional input functions with λ_1 and λ_2 increased or decreased by 10% from their initial values (see arterial glucose input function section for definitions of λ_1 and λ_2).

Animals

All animal studies were approved by the Institutional Animal Care and Use Committee at the University of Pittsburgh in accordance with the National Institutes of Health guide for the care and use of laboratory animals. All procedures were conducted in accordance ARRIVE (Animals in Research: Reporting In Vivo Experiments) guidelines (www.nc3rs.org.uk/arrive-guidelines). Animal preparation and MRI experiments have been described previously.[46,50] Adult male Fischer-344 rats (n = 4, Charles River, Wilmington, MA) weighing between 200-250 g (approx. 12 weeks of age) were anesthetized with 2% isoflurane. A burr hole was drilled into the right hemisphere at stereotaxic coordinates of 0 to 0.5 mm from bregma, and 3 to 3.5 mm from the midline. Inoculation of 100,000 to 300,000 9 L cells (ATCC CRL- 2200, Manassas, VA) in a total volume of 5 µL was performed 4 mm below the surface of the dura. After the induction of tumour cells, rats were imaged 3 to 5 weeks after (approx. age 15–17 weeks), when the tumour reached appropriate volume. Healthy adult male Sprague-Dawley (n = 3, Charles River, Wilmington, MA) rats weighing 335–388 g (approx. 12 weeks of age) were also imaged. An additional n = 3 Fischer-344 rat (254–270 g) were purchased specifically for estimation of a Fischer-344 specific population glucose input function. These animals were not scanned using MRI.

For MRI scans, rats were anesthetized with 2% isoflurane in a mixture of O_2 and air gases and the right femoral vein catheterised for delivery of glucose. After catheterisation, isoflurane levels were reduced to 1.5%. The dynamic blood pressure, end-tidal CO_2, and rectal temperature were monitored throughout the duration of the scan. The end- tidal CO_2 level was kept within 3–4% and the rectal temperature was maintained at 37.5 ± 0.1°C using a feedback-controlled heating pad. MRI data was acquired on a 9.4 T small animal MRI system (Agilent Technologies, Santa Clara, CA, USA) . Radiofrequency transmission was provided by a volume coil (6.4 cm diameter) and received by a surface coil (2.2 cm diameter; coil combination from Nova Medical, MA, USA). Spin-echo EPI CESL images with and without $R_{1\rho}$-weighting (i.e., spin-lock pulse

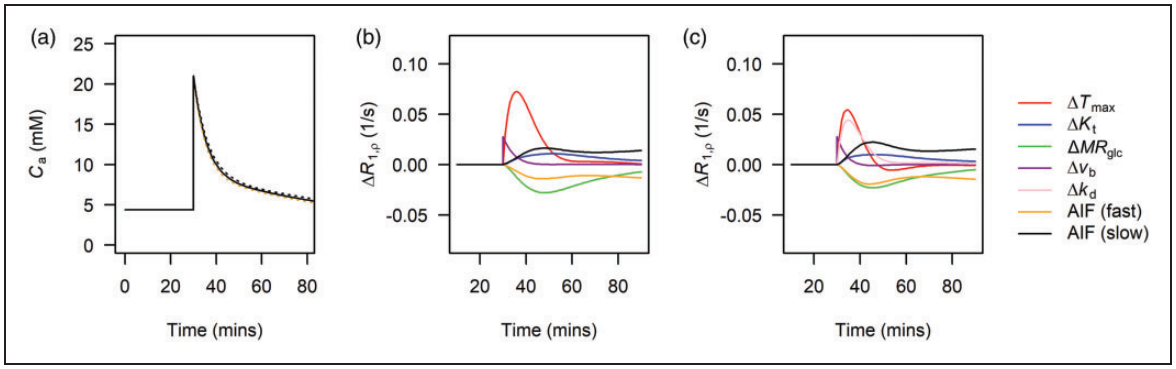

Figure 2. (a) Bi-exponential fit (solid black line) to arterial glucose input functions measured in Sprague-Dawley rats. Dashed yellow and black lines show the effect of simulating a 10% increase and decrease in both λ_1 and λ_2 of the Sprague-Dawley population-level curve reflecting faster and slower clearance of glucose from blood respectively. (b) sensitivity plots showing the effects of a 50% increase in each model parameter and increased or decreased blood glucose clearance on $\Delta R_{1\rho}$ for model 1 and (c) for model 2. While not being varied, parameters were fixed to: $T_{max}=3.3\,\mu$mol/min/mL, $K_t=8.1$ mM, $MR_{glc}=0.3\,\mu$mol/min/mL, $k_d=0.05$ mL/min/mL, $v_b=0.05$ ml/mL.

duration TSL = 0 and 50 ms) were acquired in an interleaved manner using a spin-lock frequency $\omega_1 \sim 500$ Hz. Each set of TSL = 0 ms and TSL = 50 ms images constituted a block, and were used to calculate a single $R_{1\rho}$ image as described below.

MRI data for tumour-bearing and healthy rats were acquired in two separate experiments, and some aspects have been previously reported.[46,65] The time difference between these studies meant there were some differences in the scanning and injection protocols. Table 1 shows the MRI acquisition parameters used for acquisition of tumour-bearing and healthy rat data. All experiments were performed in the non-fasted state. For tumour-bearing rats, glucose was dissolved in distilled water to 30% weight by volume concentration. For healthy rats, glucose was dissolved in distilled water to 20% weight by volume concentration. A glucose bolus (1 g/kg) was injected after 20 minutes (tumour bearing) or 30 minutes (healthy) of baseline data over approximately 30–60 seconds, after which $R_{1\rho}$ was measured for 50 minutes. $R_{1\rho}$ time-courses were estimated using the following equation:

$$R_{1\rho} = -\frac{1}{0.050\,s}\log\left(\frac{S(TSL = 0.050\,s)}{S(TSL = 0\,s)}\right)[s^{-1}] \qquad (10)$$

Arterial glucose input functions

Image-based measurement of arterial glucose concentration, C_a(t) (via measurement of $\Delta R_{1\rho}$(t)), was attempted in each rat by choosing a voxel containing only arterial blood, but results were not reliable. Instead, population level arterial input functions were derived via benchtop arterial blood sampling. For the Sprague-Dawley strain, arterial input functions were obtained the day after MRI scanning under identical experimental conditions. This data has been previously reported in Jin et al.[46] For the Fischer-344 rats, glucose input functions were not measured at the time of imaging. Three additional Fischer-344 rats were purchased specifically to measure the arterial glucose concentration timecourse, C_a(t).

For each animal, the right femoral artery was catheterized and blood samples acquired every 10 minutes (Sprague-Dawley) or 5 minutes (Fischer-344) following injection of D-glucose. As with MRI experiments, all blood sampling was performed under non-fasting conditions. The same volume, concentration, and injection rate as used during the imaging studies was used to ensure matched experimental conditions. Three blood glucose readings were acquired prior to the glucose injection and averaged to determine the baseline. Before kinetic model fitting, population input functions were smoothed by fitting a bi-exponential model with amplitude and rate parameters A_1, A_2, λ_1, λ_2.

Error analysis

Systematic error introduced into kinetic model parameters due to use of inaccurate arterial glucose input functions was determined by simulating tissue concentration curves with arterial glucose clearance rates of [A_1, A_2, $0.9\lambda_1$ $0.9\lambda_2$] and [A_1, A_2, $1.1\lambda_1$ $1.1\lambda_2$] as described above, then fitting back to the simulated curve assuming the original arterial glucose input function (i.e. using [A_1, A_2, λ_1 λ_2]). Zero mean gaussian noise with standard deviation, σ, was added to the synthetic curves to give a contrast to noise ratio ($\Delta C_{max}/\sigma$) of 30.

Kinetic model fitting

Voxelwise estimates of $\Delta R_{1\rho}$(t) were computed by subtracting the mean pre-injection $R_{1\rho}$ and converting to estimates of ΔC(t) using equation (4) and $r_g = 0.066$ $(s\,mM)^{-1}$ derived from Figure 1D of Jin et al.[46] Kinetic models were then fit to ΔC(t) time-courses using the ordinary differential equation solver ode45 and lsqcurvefit function in Matlab (Mathworks, version 5 2017a). A delay parameter was included in the fitting routine to adjust for differences in bolus arrival

Table 1. Acquisition parameters for glucoCESL experiments in tumour-bearing and healthy rats.

	Tumour bearing rats (n = 4)	Healthy rats (n = 3)
Field strength	9.4T	9.4T
Readout	Spin-echo EPI	Spin-echo EPI
Number of segment	2	1
TR	2.5s per segment	3s
TE	8.5 ms	30 ms
Field of view	$2.56 \times 2.56\,cm^2$	$3.2 \times 3.2\,cm^2$
Slice thickness	1.5 mm	2 mm
Number of slices	1 or 2 depending on size of tumour	2
Matrix size	96×96, interpolated to 128×128	64×64
Temporal resolution (block size)	30s ($2 \times$ TSL = 0, $4 \times$ TSL = 50 ms)	60 s ($5 \times$ TSL = 0, $15 \times$ TSL = 50 ms)

between the population arterial input function and uptake at tissue. Starting parameters and lower and upper limits for fitted parameters were: $T_{max} = 2$ [0, 30] μmol/min/mL, $K_t = 5$ [0, 50] mM, $MR_{glc} = 0.5$ [0, 5] μmol/min/mL, $k_d = 0.05$ [0, 10] mL/min/mL, $v_b = 0.05$ [0, 1].

In tumour-bearing rats, tumour regions of interest (ROIs) and normal tissue ROIs were outlined manually on the TSL = 0 ms image (i.e. the T_2-weighted image) in MRIcron (version 1.0.2). Normal tissue ROIs were drawn on the contralateral side, as to best match the shape and extent of the tumour ROI, but avoiding bright CSF signal. In general these ROIs covered cortical and subcortical gray matter. In healthy rats, normal tissue ROIs were drawn on both sides of the brain and summed together into a single region. These ROIs were drawn to best cover the same regions as the contralateral ROIs drawn for tumour-bearing animals. Prior to comparing tumour and normal tissue parameter values, tests for normality were performed using the Shapiro-Wilks test. The null hypothesis of normality was rejected in less than 5% of data groupings, and thus parametric tests were used throughout.

ROI-level analyses

The median value of each kinetic parameter was calculated for normal tissue and tumour ROIs. Normal tissue values in healthy rats were combined with contralateral normal tissue values from tumour-bearing rats, and the difference between tumour (n = 4) and normal tissue (n = 7) evaluated using t-tests for partially overlapping samples. To assess heterogeneity in glucose uptake and metabolism within each ROI, the standard deviation of each parameter within tumour and normal tissue ROIs was calculated[66] and the null hypothesis of no difference tested using t-tests for partially overlapping samples.

The Akaike information criterion (AIC) adjusted for small sample sizes and ΔAIC ($\Delta AIC = AIC_1 - AIC_2$) were computed on a voxelwise level to compare the fit quality between models, accounting for differences in the number of fit parameters. To test which model was preferred in tumour and normal tissue, t-tests were performed on ΔAIC to test the null hypothesis that ΔAIC = 0. A t-test for partially overlapping samples was also performed to determine if there was a difference in ΔAIC between tumour and normal tissue. Statistical analysis was done in R (version 4.0.2). Data and analysis scripts used in this paper can be obtained by request to the corresponding author.

Measurement of the $R1_\rho$ relaxivity of lactate

To assess the potential contribution of lactate to $\Delta R_{1\rho}$ we measured the $R_{1\rho}$ relaxivity of lactate in phantom at 9.4T. Lactate phantoms were created with 5 mM, 10 mM, 20 mM and 40 mM of lactate added to 1× phosphate-buffered saline and titrated to pH = 7.0. Phantoms were bundled together and heated to 37°C degree for CESL measurement. The $R_{1\rho}$ of each phantom was measured using the following spin-lock pulse parameters: $\omega_1 = 500$ Hz, varied spin-locking durations (TSL) of 0 to 1 s in 100 ms step. Images were acquired with a spin-echo EPI sequence with the following parameters: one 5-cm slice with FOV = 5 cm × 5 cm, matrix size 64 × 64, TR = 15 s, and TE = 20 ms. The relaxivity of lactate was estimated by plotting $R_{1\rho}$ vs lactate concentration and performing linear regression to find the gradient.

Results

Figure 2(a) shows how the Sprague-Dawley arterial glucose concentration varies with λ_1 and λ_2 set to 0.90 (black dashed) and 1.1 (yellow dashed), simulating slower and faster glucose clearance (for example due to slower and faster insulin responses).

Figure 2(b) and (c) show the results of the $\Delta R_{1\rho}$ sensitivity analysis for model 1 (saturable transport) and model 2 (mixed saturable transport and free diffusion) respectively. For both models, increases in T_{max}, K_t, v_b produced positive $\Delta R_{1\rho}$, whereas MR_{glc} produced negative $\Delta R_{1\rho}$. A slower glucose clearance from blood produced positive $\Delta R_{1\rho}$, and faster glucose clearance from blood produced negative $\Delta R_{1\rho}$. For both models T_{max} produced the largest change in $\Delta R_{1\rho}$ and K_t the smallest. For model 2, k_d produced an effect similar in magnitude to T_{max} but with a longer tail. For both models, v_b produced a sharp effect during the first 10 minutes post injection, which rapidly decreased with the concentration of glucose in blood. Changes in the rate of glucose clearance from blood were greater than those due to changes in K_t (both models) and MR_{glc} (model 2 only).

Figure 3 shows biases in kinetic model parameters due to use of an inaccurate arterial glucose input function. For model 1 (Figure 3(a)), biases were generally less than 40% for all parameters; biases were smallest for T_{max} (median less than ±2.6%), and largest for K_t (−2.8 to +22%), MR_{glc} (−13 to +29%), and v_b (−36% to +6%). For model 2 (Figure 3(b)), T_{max} (−17 to −9%), K_t (−12 to 11%) and v_b (−2.8 to +2.9%) were least affected, and MR_{glc} (−21 to +45%) and k_d (+12 to +27%) most affected. Errors in T_{max} and k_d were approximately equal but in opposite directions,

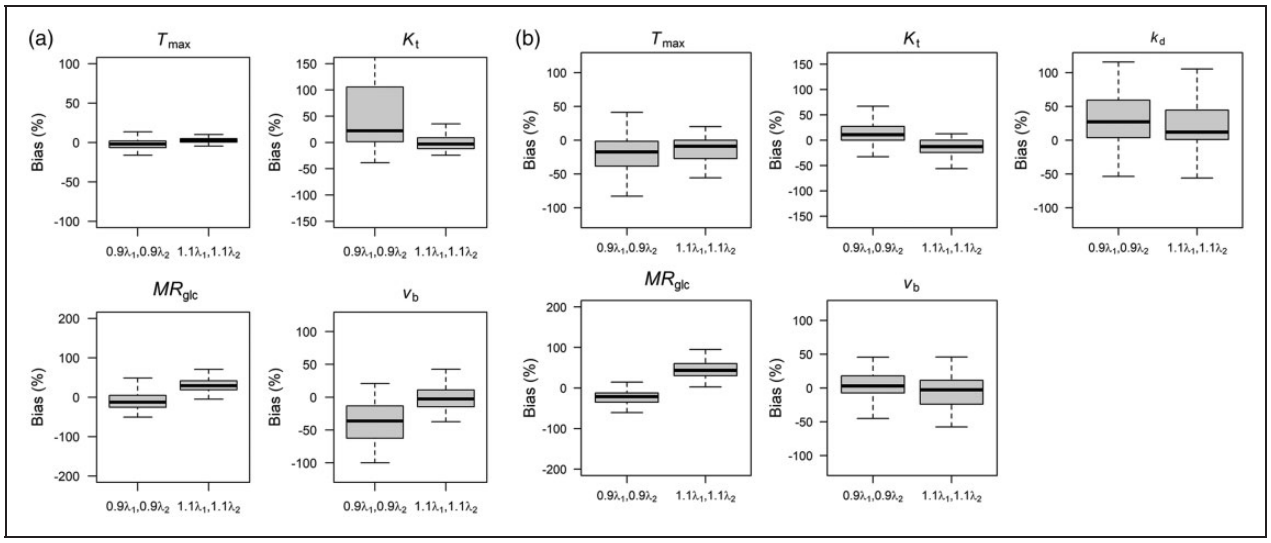

Figure 3. Bias in kinetic parameter estimates due to use of an inaccurate arterial glucose input function for (a) model 1, and (b) model 2 as displayed in Figure 2(a). Data were simulated using Sprague-Dawley input function, then kinetic models refit back to the simulated curves assuming glucose input functions with decreased ($0.9\lambda_1$) and increased ($1.1\lambda_1$) glucose clearance rates.

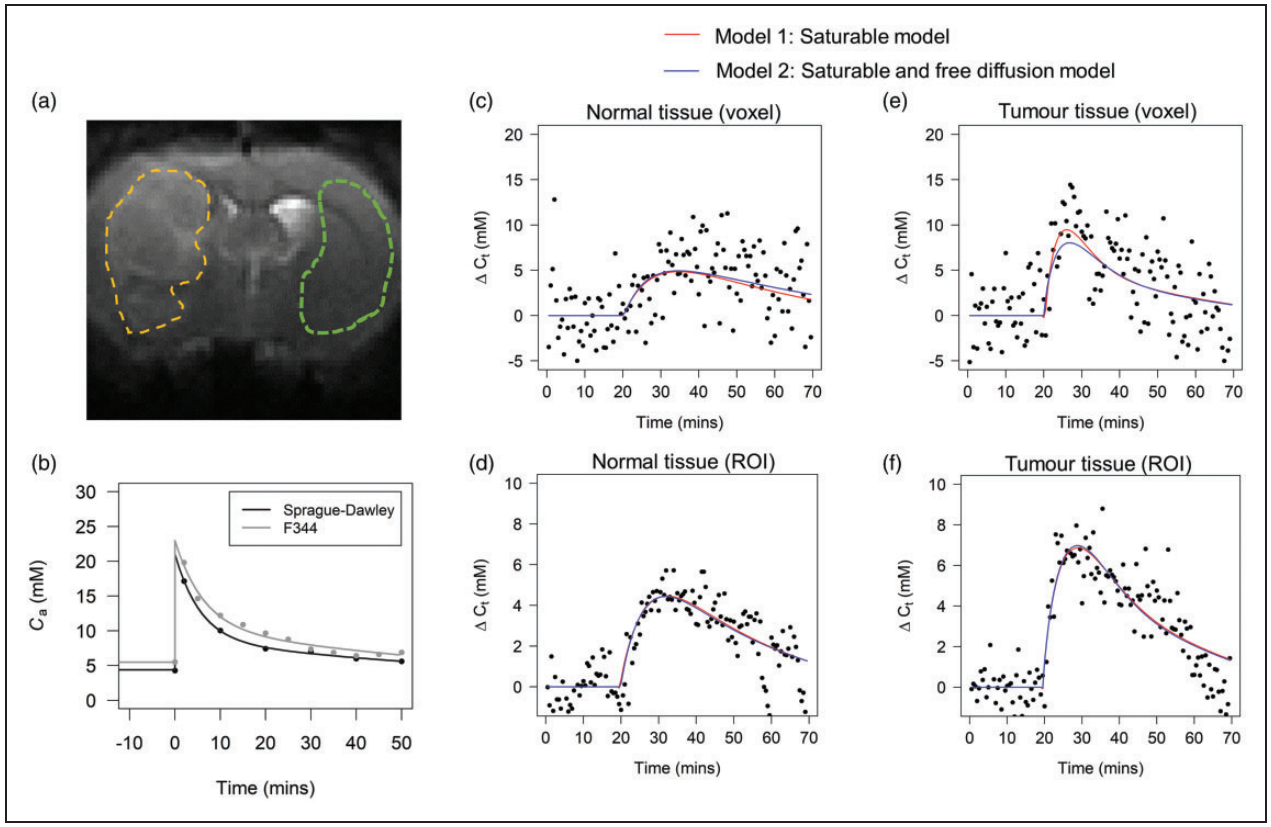

Figure 4. (a) An example CESL image acquired with TSL = 0. These images are T_2-weighted and provide excellent contrast for definition of tumour (yellow) and contralateral normal tissue (green) ROIs which were drawn manually in MRIcron. (b) Population glucose input functions for the Sprague-Daley and Fisher-344 rats. The curve shapes are similar, but the Fischer-344 curve is ~1 mM higher. Example voxelwise data and kinetic model fits in normal tissue (c) and tumour (e). Example ROI averaged data and fits in the normal tissue (d) and tumour (f). Both models provide a good fit to normal tissue and tumour data. Model 2 appears to provide a better fit to tumour data at a ROI level.

possibly reflecting degeneracy in these parameters for describing changes in $\Delta R_{1\rho}$.

Figure 4 shows an example of tumour and normal tissue region of interests (ROIs), the population-level input functions and corresponding bi-exponential fit for Sprague Dawley and Fischer-344 rats, and example voxelwise and ROI time-courses and model fits. The estimated parameters from the bi-exponential fits were $A_1 = 12.4\,\text{mM}$, $A_2 = 8.6\,\text{mM}$, $\lambda_1 = 0.18\,\text{min}^{-1}$, $\lambda_2 = 0.0086\,\text{min}^{-1}$ for Sprague-Dawley, and $A_1 = 12.5\,\text{mM}$, $A_2 = 10.4\,\text{mM}$, $\lambda_1 = 0.16\,\text{min}^{-1}$, $\lambda_2 = 0.0094\,\text{min}^{-1}$ for Fischer-344, where A_1 and A_2 are the exponential amplitudes, and λ_1 and λ_2 are the decay constants. As expected, ROI-level curves (Figures 4(d) and (f)) had higher signal to noise ratio than voxel-level curves (Figures 4(c) and (e)). In both normal and tumour tissue, model 1 and model 2 provided adequate fit at all timepoints in both voxel and ROI level data. In tumour tissue, model 2 was able to occasionally provide a more accurate description of the peak of the curve (Figure 4E).

Figure 5 shows spatial maps of each kinetic parameter for a tumour bearing rat, and mean values (±sd) of each kinetic parameter averaged across all rats in normal (n = 7) and tumour tissue (n = 4). P-values show the results of t-tests comparing mean parameters in normal tissue and tumour. Mean values ± sd and p-values are also given for each parameter in Table 2. The difference in AIC between model 1 and model 2 in normal tissue and tumour is also shown as a parameter

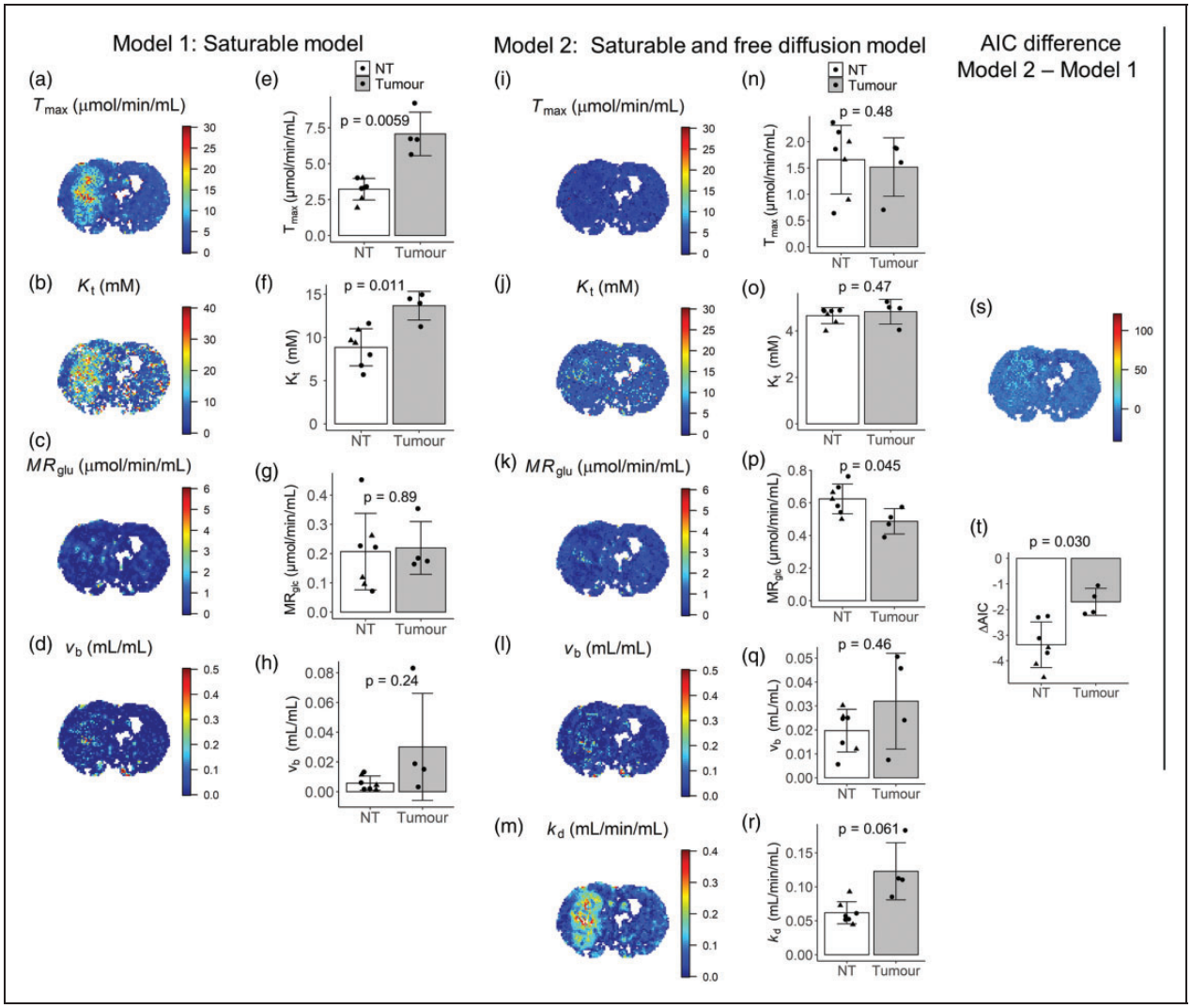

Figure 5. GlucoCESL parameter maps from a tumour bearing rat using model 1 (a–d) and model 2 (i–m), and mean parameter values in normal tissue (healthy – triangle; tumour bearing – circle; n = 7) and tumour (n = 4) for model 1 (e–h) and model 2 (n–r). Far right is the corresponding ΔAIC map (s) and mean ΔAIC in normal tissue and tumour (t). T-tests for partially overlapping samples were used to test the null hypothesis of no difference in parameter values between normal tissue and tumour. Error bars show group standard deviation.

Table 2. Estimates of mean ± sd for kinetic parameters from model 1 and model 2, and results from Partover t-tests between estimates in normal tissue and tumour.

	Model 1 (saturable transport)			Model 2 (saturable and free diffusion)		
	Normal tissue (n = 7)	Tumour (n = 4)	p-value	Normal tissue (n = 7)	Tumour (n = 4)	p-value
T_{max} (μmol/min/mL)	3.2 ± 0.6	7.1 ± 2.7	0.0059	1.7 ± 0.67	1.5 ± 0.56	0.48
K_t (mM)	8.8 ± 2.2	14 ± 1.7	0.011	4.7 ± 0.34	4.8 ± 0.53	0.47
MR_{glc} (μmol/min/mL)	0.21 ± 0.13	0.22 ± 0.09	0.89	0.61 ± 0.090	0.48 ± 0.078	0.045
v_b (mL/mL)	0.0057 ± 0.0048	0.030 ± 0.035	0.24	0.022 ± 0.0087	0.031 ± 0.020	0.46
k_d (mL/min/mL)				0.061 ± 0.017	0.12 ± 0.042	0.061

map (Figure 5(s)), and summarised across all rats as a barplot (Figure 5(t)). Visually, both models produce high fidelity maps of transport and metabolic parameters. For model 1, normal tissue/tumour contrast can be observed in images of T_{max} and K_t, whereas little or no contrast is observed for MR_{glc} and v_b. This is reflected in the group comparisons. There were significant differences between tumour and normal tissue for T_{max} (54% increase; $p = 0.0059$) and K_t (40% increase; $p = 0.011$). On the contrary, there was no significant difference in MR_{glc}. When evaluating model 2 parameters, there was a borderline significant reduction in MR_{glc} in tumour tissue (21% reduction; $p = 0.045$), and a borderline significant increase in k_d (49% increase; $p = 0.061$). Model 2 estimates of T_{max}, K_t, and v_b were unchanged between tumour and normal tissue. Averaged across all animals, the difference in AIC between models (AIC model 1–AIC model 2) was significantly less than zero for both normal tissue and tumour tissue ($\Delta AIC < 0$; $p = 4.1 \times 10^{-5}$ and $p = 0.0076$ for normal and tumour tissue respectively).

Supplementary Figure 1 shows the standard deviation of glucose uptake and metabolic parameters in tumour and normal tissue ROIs. There was no differences in the standard deviation of parameters between normal and tumour tissue except for v_b from model 1 ($p = 0.016$; greater sd in tumour tissue), and k_d from model 2 ($p = 0.014$; greater sd in tumour tissue).

Supplementary Figure 2 shows how $R_{1\rho}$ varies with lactate concentration in phantom. The $R_{1\rho}$ relaxivity of lactate was found to be 0.0018 $(s\ mM)^{-1}$.

Discussion

We have presented the theory for quantitative kinetic modelling of glucoCESL MRI data, and applied two kinetic models to data from tumour-bearing and healthy rats. Parameter estimates from both models agree well with previously published values.[31] Mason et al. summarised NMR spectroscopy estimates of T_{max}, K_t, and k_d in rat brain from 19 prior studies. In studies that used model 1 (n = 14), estimates of T_{max} and K_t were 3.9 ± 0.5 μmol/min/mL (assuming 0.83 mL water/g tissue) and 8.1 ± 0.6 mM which agree well with our normal tissue estimates of 3.2 ± 0.62 μmol/min/mL and 8.8 ± 2.2 mM. In studies that used model 2 (n = 5), estimates of T_{max}, K_t, and k_d were 1.56 ± 0.61 μmol/min/mL, 6.8 ± 0.6 mM, and $k_d = 0.025 \pm 0.0074$ mL/min/mL, which also agree well with our normal tissue estimates from model 2 of $T_{max} = 1.7 \pm 0.67$ μmol/min/mL, $K_t = 4.7 \pm 0.34$ mM and $k_d = 0.061 \pm 0.017$ mL/min/mL. While there is greater discrepancy between model 2 parameters and available literature data than for model 1, the direction of change in T_{max} and K_t when using model 2 versus model 1 is consistent (i.e. both are reduced), indicating that our data is also consistent with prior studies.

Model 1 estimates of MR_{glc} in normal tissue (0.21 ± 0.13 μmol/min/mL) were also within the range of previously published values. In laboratory rats, the effects of anesthesia on MR_{glc} are profound, and must be considered when comparing MR_{glc} between studies.[67] In fasted rats anesthetised with 2% isoflurane, Du et al. measured MR_{glc} in a large region covering the cortex and subcortical brain and found values of 0.53 ± 0.20 μmol/min/mL.[28] Lu et al. used similar anaesthesia and deuterium spectroscopic imaging of deuterated glucose in unfasted rat, and found MR_{glc} values in whole rat brain of 0.28 ± 0.13 μmol/min/g.[38] Shimoji et al. used FDG-PET scanning and halothane anesthesia (1–1.5%) in fasted rat to estimate MR_{glc} in the cortex and found values of 0.24 ± 4.8 μmol/min/g.[68] Suzuki et al. investigated the effects of different anesthesia on MR_{glc} using FDG-PET, including scanning of conscious rat. In conscious rat, much higher values of 0.93 ± 0.18 μmol/min/g were reported, which reduced to 0.54 ± 16 μmol/min/g with isoflurane anesthesia.[67] Similarly, conscious rat values for MR_{glc} obtained by Hawkin's et al. using the autoradiographic technique were of the order of 1.1–1.2 μmol/min/g.[64] Thus, our values for MR_{glc} certainly lie within the range of previously published values for MR_{glc} in anesthetised rats.

Model 2 estimates of MR_{glc} (0.61 ± 0.009 μmol/min/mL) were approximately 3 times higher than MR_{glc}

estimates made using model 1 (0.21 ± 0.13 μmol/min/mL). It is possible that the introduction of the additional k_d parameter could lead to more accurate modelling of glucose influx/efflux, leading to more accurate estimation of MR_{glc}. We assessed other studies using model 2 to determine if MR_{glc} was affected. Pardridge et al. used pentabarbitol anesthetisia and found MR_{glc} values in cortex of 0.28 μmol/min/mL.[69] Crane et al. also used pentabarbitol anesthesia but also studied conscious rat and found values of MR_{glc} of 0.27 μmol/min/g[21] and 1.02 μmol/min/g respectively. Cremer studied conscious rat only and found values of 1.24 μmol/min/mL.[70] While data is not available on isoflurane-anesthetised rats, all these values are not substantially different from literature values using model 1 indicating that model 2 estimates of MR_{glc} should not be affected substantially by modelling of free diffusion, particularly in tissues with intact BBB. It is therefore important that further work is done to validate model 2 estimates of MR_{glc} obtained using glucoCESL MRI.

The maximal transport capacity (T_{max}) and the half saturation constant (K_t) from model 1 were significantly higher in tumour than normal tissue, indicating increased uptake of glucose. Higher T_{max} may reflect an increased density of glucose transporters on the vasculature and tumour cell membranes. However, in the context of increased K_t, the interpretation must be carefully considered. K_t will trade-off saturable and non-saturable kinetics, and as K_t increases, K_1 becomes less dependent on C_a, and begins to mimic the behaviour of the free diffusion constant k_d. Thus, increased T_{max} and K_t together may reflect the presence of free diffusion and blood-brain barrier breakdown. This interpretation is supported by model 2 parameters, where differences in T_{max} and K_t between tumour and normal tissue do not exist or are much smaller, and variability in uptake of glucose is described mainly by k_d (Figure 5 (a), (b), (i), (j) and (m)). We did not find any difference in metabolic rate of glucose consumption between tumours and normal tissue for model 1, which is consistent with the clinical observation that uptake of FDG in many brain tumours is often no higher than surrounding normal tissue.[16] On the contrary, a small but significant reduction in model 2 MR_{glc} was observed in tumour tissue. However, given the uncertainty associated with model 2 estimates of MR_{glc} as described previously, this result should be treated with caution until verified by further studies. Model 1 and model 2 predicted no difference in blood volume between normal tissue and tumour. Model 1 estimates of blood volume were much lower than known values ($v_b < 0.005$ mL/mL and $v_b < 0.01$ mL/mL for normal tissue and tumour respectively). Estimates for model 2 were more reasonable but still low ~ 0.02–0.03 mL/mL. The underestimation could be a result of the shorter T_2 of the blood compartment relative to tissue at 9.4 T[71] which might cause glucose in the blood compartment to be less visible than glucose in tissue.

Estimates of the Akaike information criterion (AIC) in normal and tumour tissue showed that model 1 had significantly lower AIC than model 2 ($\Delta AIC < 0$; $p = 4.1 \times 10^{-5}$ and $p = 0.0076$ for normal and tumour tissue respectively), indicating that the additional free diffusion parameter of model 2 did not describe any additional variability above that described by model 1. This does not mean that model 2 is less accurate or did not fit the data as well as model 1, but that within the conditions of our experiment (i.e. temporal resolution, SNR), the additional parameter did not provide additional predictive power over parameters already present in model 1. It is clear from our results that the normal tissue values of transport and metabolic parameters from model 1 are more consistent with literature values. It was also shown in previous work that the same tumour-bearing rats as scanned in this study exhibit leakage of DCE-MRI contrast agents (see Figure 3C of Jin et al.[65]) indicative of BBB breakdown. This suggests model 2 may more appropriately ascribe changes in glucose uptake in tumour tissue to free diffusion rather than changes to saturable transport mechanisms. Further validation work is needed to confirm these points.

We have assumed that contributions from metabolic products of glucose to $\Delta R_{1\rho}$ were negligible compared to the effects of glucose itself. It is shown in previous work that changes in concentrations of glucose-6-phosphate[58] and neurotransmitters such as glutamate[59] are very small, and should not affect $\Delta R_{1\rho}$. Since tumours can produce high levels of lactate, we performed an additional phantom study to demonstrate that rising lactate levels will also not appreciably affect $\Delta R_{1\rho}$. The $R_{1\rho}$ relaxivity of lactate was found to be 0.0018 $(s\ mM)^{-1}$, 37 times smaller than glucose. Using the reported values of the chemical shift and exchange of lactate from recent literature,[60] predicted $R_{1\rho}$ relaxivity is even smaller than our measured value (~ 0.0005 $(s\,mM)^{-1}$, 134 times smaller than glucose). It is not yet clear what effects lactate will have on CEST detection, which is more sensitive to slower exchange rates than CESL. Changes to $\Delta R_{1\rho}$ from osmolality effects and differences in tissue pH were also ignored, which may have a larger effect on $\Delta R_{1\rho}$.[50] These factors, and the impact of a wider range of metabolites, should be investigated in future work to further refine the modelling approach.

The study has the following limitations. We have used a population-based arterial glucose input function instead of using individually sampled, or image-derived arterial input functions. We attempted to obtain image-derived AIFs from the carotid artery, but it was not possible to obtain reliable results. This is presumably

due to inflow of fresh unsaturated blood into the imaging slice (i.e. blood that has not undergone spin-locking) during the time between spin-locking and the SE-EPI readout. It is possible the shape of the population level curves may have deviated from the true (individual) input function of the rats investigated in this study. Our simulations showed that deviations between assumed and true arterial glucose concentrations can have appreciable effects on $\Delta R_{1\rho}$, particularly at later time points (the peak effect was observed ~20 minutes post glucose injection), which then propagate through to biases in estimates of all kinetic parameters, but predominantly affected K_t, MR_{glc}, and v_b for model 1 and MR_{glc} and k_d for model 2. These results highlight the importance of accurate input function characterisation when using such models, particularly for inter-subject or group-level comparisons. Accurate knowledge of input functions may not be so important for intra-subject comparisons (e.g. tumour vs normal tissue) as it could be expected the glucose input to different brain regions will be similar. Despite the potential for large biases, the excellent correspondence between our kinetic parameter estimates (particularly for model 1) and literature values suggest that the input functions used in this work are an accurate representation of the true arterial glucose time-courses. Future work should investigate the use of CESL and CEST approaches for measuring an image-derived input functions, and/or further validate the accuracy of the population based input function approach for group level comparisons. It is possible that adjustment (e.g. scaling) of population level input functions using pre- and post-scan venous blood glucose measurements (e.g. using a simple blood glucose monitor) may be adequate to account for inter-individual or group variability in blood glucose concentration time-courses. There were some small differences in the acquisition parameters and injection protocols between tumour bearing and healthy rats. For example, the weight by volume concentration, and hence the administered volumes of glucose solution were different. It is possible these effects led to small differences in osmolality of blood. However, given the estimated kinetic parameter values for normal tissue in healthy and tumour bearing rats were not appreciably different, we are confident these effects were small. For future glucose-enhanced MRI studies, including translational work in humans, a standardised set of optimal acquisition parameters are needed.

To conclude, we have for the first time demonstrated the feasibility of applying kinetic models to glucoCESL MRI data and show the potential of the approach to probe glucose transport and metabolism *in-vivo* at high spatial resolution.

Funding

The work was funded by the Engineering and Physical Research Council grants EP/M005909/1 and EP/S031510/1, Medical Research Council Confidence in Concept Funding [Round 6, MC_PC_17172] (Manchester) and NIH grant NS100703.

Declaration of conflicting interests

The author(s) declared the following potential conflicts of interest with respect to the research, authorship, and/or publication of this article: GJMP is a shareholder and director of Bioxydyn Limited, a company with an interest in quantitative imaging biomarkers. He is also a shareholder and Director of Queen Square Analytics, a company with an interest in MRI applied to neuroscience.

Authors' contributions

BD conducted the research and drafted the manuscript. RH, GP, LP, and JM supervised the research. TJ shared the data and provided technical input into data analysis. HB, WH, and PW acquired benchtop glucose input functions. All authors edited and approved the submitted version.

Acknowledgments

We would like to thank Professor Stephen Williams for invaluable discussions regarding the work and early manuscript drafts.

ORCID iDs

Ben R Dickie https://orcid.org/0000-0001-5018-2111
Rainer Hinz https://orcid.org/0000-0002-7808-9207
William Harris https://orcid.org/0000-0002-7994-1166
Hervé Boutin https://orcid.org/0000-0002-0029-5246
Laura M Parkes https://orcid.org/0000-0001-6488-507X

Supplemental material

Supplemental material for this article is available online.

References

1. Denko NC. Hypoxia, HIF and metabolism in the solid tumour. *Nat Rev Cancer* 2008; 8: 705–713.
2. Butterfield DA and Halliwell B. Oxidative stress, dysfunctional glucose metabolism and Alzheimer disease. *Nat Rev Neurosci* 2019; 20: 148–160.
3. Peppard RF, Martin WRW, Schulzer M, et al. Cerebral glucose metabolism in Parkinson's disease with and without dementia. *Arch Neurol* 1992; 49: 1262–1268.
4. Eberling JL, Richardson BC, Reed BR, et al. Cortical glucose metabolism in Parkinson's disease without dementia. *Neurobiol Aging* 1994; 15: 329–335.
5. Roelcke U, Kappos L, Lechner-Scott J, et al. Reduced glucose metabolism in the frontal cortex and basal ganglia of multiple sclerosis patients with fatigue: a 18F-fluorodeoxyglucose positron emission tomography study. *Neurology* 1997; 48: 1566–1571.
6. Bakshi R, Miletich RS, Kinkel PR, et al. High-resolution fluorodeoxyglucose positron emission tomography shows

both global and regional cerebral hypometabolism in multiple sclerosis. *J Neuroimaging* 1998; 8: 228–234.
7. Kyrtata N, Emsley HCA, Sparasci O, et al. A systematic review of glucose transport alterations in Alzheimer's disease. *Front Neurosci* 2021; 15: 1–15.
8. Lund-Andersen H. Transport of glucose from blood to brain. *Physiol Rev* 1979; 59: 305–352.
9. Boado RJ, Black KL and Pardridge WM. Gene expression of GLUT3 and GLUT1 glucose transporters in human brain tumors. *Mol Brain Res* 1994; 27: 51–57.
10. Airley R, Loncaster J, Davidson S, et al. Glucose transporter glut-1 expression correlates with tumor hypoxia and predicts metastasis-free survival in advanced carcinoma of the cervix. *Clin Cancer Res* 2001; 7: 928–934.
11. Yeh W-L, Lin C-J and Fu W-M. Enhancement of glucose transporter expression of brain endothelial cells by vascular endothelial growth factor derived from glioma exposed to hypoxia. *Mol Pharmacol* 2008; 73: 170–177.
12. Simpson IA, Chundu KR, Davies-Hill T, et al. Decreased concentrations of GLUT1 and GLUT3 glucose transporters in the brains of patients with Alzheimer's disease. *Ann Neurol* 1994; 35: 546–551.
13. Iadecola C. Sugar and Alzheimer's disease: a bittersweet truth. *Nat Neurosci* 2015; 18: 477–478.
14. Winkler EA, Nishida Y, Sagare AP, et al. GLUT1 reductions exacerbate Alzheimer's disease vasculo-neuronal dysfunction and degeneration. *Nat Neurosci* 2015; 18: 521–530.
15. Mosconi L, Tsui WH, Herholz K, et al. Multicenter standardized 18F-FDG PET diagnosis of mild cognitive impairment, Alzheimer's disease, and other dementias. *J Nucl Med* 2008; 49: 390–398.
16. Chen W. Clinical applications of PET in brain tumors. *J Nucl Med* 2007; 48: 1468–1481.
17. Gjedde A. Calculation of cerebral glucose phosphorylation from brain uptake of glucose analogs in vivo: a re-examination. *Brain Res Rev* 1982; 4: 237–274.
18. Gejl M, Egefjord L, Lerche S, et al. Glucagon-like peptide-1 decreases intracerebral glucose content by activating hexokinase and changing glucose clearance during hyperglycemia. *J Cereb Blood Flow Metab* 2012; 32: 2146–2152.
19. Sokoloff L, Reivich M, Kennedy C, et al. The [14C]deoxyglucose method for the measurement of local cerebral glucose utilization: theory, procedure, and normal values in the conscious and anesthetized albino rat. *J Neurochem* 1977; 28: 897–916.
20. Hasselbalch SG, Madsen PL, Knudsen GM, et al. Calculation of the FDG lumped constant by simultaneous measurements of global glucose and FDG metabolism in humans. *J Cereb Blood Flow Metab* 1998; 18: 154–160.
21. Crane PD, Pardridge WM, Braun LD, et al. Kinetics of transport and phosphorylation of 2-fluoro-2-deoxy-d-glucose in rat brain. *J Neurochem* 1983; 40: 160–167.
22. Tokugawa J, Ravasi L, Nakayama T, et al. Operational lumped constant for FDG in normal adult male rats. *J Nucl Med* 2007; 48: 94–99.
23. Reivich M, Alavi A, Wolf A, et al. Glucose metabolic rate kinetic model parameter determination in humans: the lumped constants and rate constants for [18F] fluorodeoxyglucose and [11C]deoxyglucose. *J Cereb Blood Flow Metab* 1985; 5: 179–192.
24. Graham MM, Muzi M, Spence AM, et al. The FDG lumped constant in normal human brain. *J Nucl Med* 2002; 43: 1157–1166.
25. Hasselbalch SG, Knudsen GM, Holm S, et al. Transport of D-glucose and 2-fluorodeoxyglucose across the blood-brain barrier in humans. *J Cereb Blood Flow Metab* 1996; 16: 659–666.
26. Michaelis T, Merboldt K-D, Hänicke W, et al. On the identification of cerebral metabolites in localized 1H NMR spectra of human brain in vivo. *NMR Biomed* 1991; 4: 90–98.
27. Gruetter R, Novotny EJ, Boulware SD, et al. 1H NMR studies of glucose transport in the human brain. *J Cereb Blood Flow Metab* 1996; 16: 427–438.
28. Du F, Zhang Y, Zhu X-H, et al. Simultaneous measurement of glucose blood–brain transport constants and metabolic rate in rat brain using in-vivo 1H MRS. *J Cereb Blood Flow Metab* 2012; 32: 1778–1787.
29. Gruetter R, Garwood M, Uğurbil K, et al. Observation of resolved glucose signals in 1H NMR spectra of the human brain at 4 Tesla. *Magn Reson Med* 1996; 36: 1–6.
30. Gruetter R, Adriany G, Choi I-Y, et al. Localized in vivo 13C NMR spectroscopy of the brain. *NMR Biomed* 2003; 16: 313–338.
31. Mason GF, Behar KL, Rothman DL, et al. NMR determination of intracerebral glucose-concentration and transport kinetics in rat-brain. *J Cereb Blood Flow Metab* 1992; 12: 448–455.
32. van Zijl PCM, Davis D, Eleff SM, et al. Determination of cerebral glucose transport and metabolic kinetics by dynamic MR spectroscopy. *Int J Pediatr Otorhinolaryngol* 2000; 54: 77.
33. Choi IY, Lee SP, Kim SG, et al. In vivo measurements of brain glucose transport using the reversible Michaelis-Menten model and simultaneous measurements of cerebral blood flow changes during hypoglycemia. *J Cereb Blood Flow Metab* 2001; 21: 653–663.
34. Gruetter R, Novotny EJ, Boulware SD, et al. Direct measurement of brain glucose concentrations in humans by 13C NMR spectroscopy. *Proc Natl Acad Sci U S A* 1992; 89: 1109–1112.
35. De Graaf RA, Pan JW, Telang F, et al. Differentiation of glucose transport in human brain gray and white matter. *J Cereb Blood Flow Metab* 2001; 21: 483–492.
36. Klomp DWJ, Renema WKJ, Van Der Graaf M, et al. Sensitivity-enhanced 13C MR spectroscopy of the human brain at 3 Tesla. *Magn Reson Med* 2006; 55: 271–278.
37. De Feyter HM, Behar KL, Corbin ZA, et al. Deuterium metabolic imaging (DMI) for MRI-based 3D mapping of metabolism in vivo. *Sci Adv* 2018; 4: 1–12.
38. Lu M, Zhu XH, Zhang Y, et al. Quantitative assessment of brain glucose metabolic rates using in vivo deuterium magnetic resonance spectroscopy. *J Cereb Blood Flow Metab* 2017; 37: 3518–3530.
39. Kreis F, Wright AJ, Hesse F, et al. Measuring tumor glycolytic flux in vivo by using fast deuterium MRI. *Radiology* 2020; 294: 289–296.

40. Valette J, Tiret B and Boumezbeur F. Experimental strategies for in vivo 13C NMR spectroscopy. *Anal Biochem* 2017; 529: 216–228.
41. Wolff SD and Balaban RS. NMR imaging of labile proton exchange. *J Magn Reson* 1990; 86: 164–169.
42. Zhou J, Wilson DA, Sun PZ, et al. Quantitative description of proton exchange processes between water and endogenous and exogenous agents for WEX, CEST, and APT experiments. *Magn Reson Med* 2004; 51: 945–952.
43. Chan KWY, McMahon MT, Kato Y, et al. Natural D -glucose as a biodegradable MRI contrast agent for detecting cancer. *Magn Reson Med* 2012; 68: 1764–1773.
44. Walker-Samuel S, Ramasawmy R, Torrealdea F, et al. In vivo imaging of glucose uptake and metabolism in tumors. *Nat Med* 2013; 19: 1067–1072.
45. Nasrallah FA, Pagès G, Kuchel PW, et al. Imaging brain deoxyglucose uptake and metabolism by glucoCEST MRI. *J Cereb Blood Flow Metab* 2013; 33: 1270–1278.
46. Jin T, Mehrens H, Hendrich KS, et al. Mapping brain glucose uptake with chemical exchange-sensitive spin-lock magnetic resonance imaging. *J Cereb Blood Flow Metab* 2014; 34: 1402–1410.
47. Paech D, Schuenke P, Christina K, et al. T1rho-weighted dynamic glucose-enhanced MR imaging in the human brain. *Radiology* 2017; 285: 914–922.
48. Schuenke P, Koehler C, Korzowski A, et al. Adiabatically prepared spin-lock approach for T1ρ-based dynamic glucose enhanced MRI at ultrahigh fields. *Magn Reson Med* 2017; 78: 215–225.
49. Zaiss M, Ehses P and Scheffler K. Snapshot-CEST: optimizing spiral-centric-reordered gradient echo acquisition for fast and robust 3D CEST MRI at 9.4 T. *NMR Biomed* 2018; 31: 1–14.
50. Jin T, Mehrens H, Wang P, et al. Chemical exchange-sensitive spin-lock MRI of glucose analog 3-O-methyl-D-glucose in normal and ischemic brain. *J Cereb Blood Flow Metab* 2018; 38: 869–880.
51. Boyd PS, Breitling J, Zimmermann F, et al. Dynamic glucose-enhanced (DGE) MRI in the human brain at 7 T with reduced motion-induced artifacts based on quantitative $R1_\rho$ mapping. *Magn Reson Med* 2020; 84: 182–191.
52. Huang J, van Zijl PCM, Han X, et al. Altered d-glucose in brain parenchyma and cerebrospinal fluid of early Alzheimer's disease detected by dynamic glucose-enhanced MRI. *Sci Adv* 2020; 6: eaba3884.
53. Chen L, Wei Z, Chan KWY, et al. D-glucose uptake and clearance in the tauopathy Alzheimer's disease mouse brain detected by on-resonance variable delay multiple pulse MRI. *J Cereb Blood Flow Metab* 2021; 41: 1013–1025.
54. Rivlin M and Navon G. CEST MRI of 3-O-methyl-D-glucose on different breast cancer models. *Magn Reson Med* 2018; 79: 1061–1069.
55. Zu Z, Spear J, Li H, et al. Measurement of regional cerebral glucose uptake by magnetic resonance spin-lock imaging. *Magn Reson Imaging* 2009; 6: 247–253.
56. Sehgal AA, Li Y, Lal B, et al. CEST MRI of 3-O-methyl-D-glucose uptake and accumulation in brain tumors. *Magn Reson Med* 2019; 81: 1993–2000.
57. Aleshin AE, Zeng C, Bourenkov GP, et al. The mechanism of regulation of hexokinase: new insights from the crystal structure of recombinant human brain hexokinase complexed with glucose and glucose-6-phosphate. *Structure* 1998; 6: 39–50.
58. Van Zijl PCM, Davis D, Eleff SM, et al. Determination of cerebral glucose transport and metabolic kinetics by dynamic MR spectroscopy. *Am J Physiol* 1997; 273: E1216–E1227.
59. Xu X, Xu J, Chan KWY, et al. GlucoCEST imaging with on-resonance variable delay multiple pulse (onVDMP) MRI. *Magn Reson Med* 2019; 81: 47–56.
60. DeBrosse C, Nanga RPR, Bagga P, et al. Lactate chemical exchange saturation transfer (LATEST) imaging in vivo a biomarker for LDH activity. *Sci Rep* 2016; 6: 1–10.
61. Purich DL and Fromm HJ. The kinetics and regulation of rat brain hexokinase. *J Biol Chem* 1971; 246: 3456–3463.
62. Pardridge WM and Oldendorf WH. Transport of metabolic substrates through the blood-brain barrier. *J Neurochem* 1977; 28: 5–12.
63. Sourbron SP and Buckley DL. On the scope and interpretation of the Tofts models for DCE-MRI. *Magn Reson Med* 2011; 66: 735–745.
64. Hawkins R, Hass WK and Ransohoff J. Measurement of regional brain glucose utilization in vivo using [2-14C] glucose. *Stroke* 1979; 10: 690–702.
65. Jin T, Iordanova B, Hitchens TK, et al. Chemical exchange–sensitive spin-lock (CESL) MRI of glucose and analogs in brain tumors. *Magn Reson Med* 2018; 80: 488–495.
66. Just N. Improving tumour heterogeneity MRI assessment with histograms. *Br J Cancer* 2014; 111: 2205–2213.
67. Suzuki C, Kosugi M and Magata Y. Conscious rat PET imaging with soft immobilization for quantitation of brain functions: comprehensive assessment of anesthesia effects on cerebral blood flow and metabolism. *EJNMMI Res* 11. Epub ahead of print 2021; DOI: 10.1186/s13550-021-00787-6.
68. Shimoji K, Ravasi L, Schmidt K, et al. Measurement of cerebral glucose metabolic rates in the anesthetized rat by dynamic scanning with 18F-FDG, the ATLAS small animal PET scanner, and arterial blood sampling. *J Nucl Med* 2004; 45: 665–672.
69. Pardridge WM, Crane PD, Mietus LJ, et al. Kinetics of regional blood–brain barrier transport and brain phosphorylation of glucose and 2-deoxyglucose in the barbiturate–anesthetized rat. *J Neurochem* 1982; 38: 560–568.
70. Cremer JE, Cunningham VJ and Seville MP. Relationships between extraction and metabolism of glucose, blood flow, and tissue blood volume in regions of rat brain. *J Cereb Blood Flow Metab* 1983; 3: 291–302.
71. Dickie BR, Parker GJM and Parkes LM. Measuring water exchange across the blood-brain barrier using MRI. *Prog Nucl Magn Reson Spectrosc* 2020; 116: 19–39.